Low-order modelling and sensor-based prediction of stalled airfoils at moderate Reynolds number

Douglas W. Carter and Bharathram Ganapathisubramani
Dept. of Aeronautical & Astronautical Engineering
University of Southampton, Southampton, UK, SO17 1BJ

We present analysis from planar time-resolved particle image velocimetry (PIV) fields in the stream-wise surface-normal plane of turbulent flow surrounding NACA 0012 and NACA 65-410 airfoils at $Re_c \approx 7 \times 10^4$ focusing on static stall phenomena at intermediate to high angles of attack α. Dominant flow frequencies, identified from the lift spectra obtained from a load cell mounted to the foils, highlight the presence of bluff-body shedding ($f^\star_\alpha = f \frac{c}{U_\infty} \sin\alpha$ of O(10^{-1}) where f is the frequency, c the airfoil chord, and U_∞ the freestream velocity) for all cases and prominent low frequencies ($f^\star_\alpha$ of O(10^{-2})) for cases in transient stall (TS). A data-driven modelling framework via the proper orthogonal decomposition (POD) reveals the low-frequencies are associated to flow separation and reattachment driven by underlying expansion and contraction normal to the suction surface. Further, the ability to predict the low-order features from (pseudo) pressure probes at the leading, mid-chord, and trailing edges for both TS and deep stall (DS) cases is quantified using linear stochastic estimation (LSE). The framework pinpoints the centroid of the region of reverse flow with error on the order of 5 and 20% for DS and TS regimes, respectively. Notably, it is found that LSE coefficients governing the low-order POD correlations do not strongly depend on the airfoil geometry. This is demonstrated by the comparative performance of training the LSE using the probes of the NACA 0012 cases to predict the NACA 65-410 velocity fields and vice-versa. This work demonstrates the insight afforded by the POD on the low-order features of turbulent stalled airfoils as well as the similarity of such features across geometries towards predicting flow features for potentially any airfoil geometry without the need to re-train an LSE library.

Nomenclature

A = Attached
DAQ = Data Acquisition Device
DS = Deep Stall
LE = Leading Edge

LSE = Linear Stochastic Estimation

xLSE = Cross Linear Stochastic Estimation

Nd:YLF = Nyodymium-doped Yttrium Lithium Fluoride

PIV = Particle Image Velocimetry

POD = Proper Orthogonal Decomposition

RANS = Reynolds-averaged Navier-Stokes

TA = Thin-airfoil

TE = Trailing edge

TKE = Planar turbulent kinetic energy

TS = Transient Stall

A_k = Model mode amplitude

a_k = Temporal POD coefficient

a_k^* = Estimated POD coefficient (LSE)

a_k^x = Estimated POD coefficient (xLSE)

$\hat{a}_k$ = Modelled temporal POD coefficient

c = Airfoil chord length [cm]

C_L = Lift coefficient

C_p = Pressure coefficient

$e(a_k)$ = Error of estimated POD coefficients

e_c = Centroid reconstruction error

f = Frequency [Hz]

$f^\star$ = Airfoil chord based normalized frequency based

$f_\alpha^\star$ = Cross-stream airfoil chord projection based normalized frequency

k = POD mode index

k_0 = Reference POD mode index

L = Lift force [N]

p = Instantaneous pressure field [Pa]

p' = Fluctuating pressure field [Pa]

P = Mean pressure field [Pa]

Re_c = Chord-based Reynolds number

s = Submerged airfoil span [cm]

s_{tot} = Total airfoil span [cm]

$St^\star$ = Strouhal frequency

$St^\star_{min}$ = Minimum Strouhal frequency

t = Time [s]

T = Eddy turnover time scale [s]

$T^\star$ = Normalized model time scale

u_i = Instantaneous velocity vector field [m/s]

$\hat{u}_i$ = Model instantaneous velocity vector field [m/s]

u'_i = Fluctuating velocity vector field [m/s]

U_i = Mean velocity vector field [m/s]

U_∞ = Free-stream velocity [m/s]

V_{ij} = Probe-mode cross-correlation matrix

W_{ij} = Probe correlation matrix

α = Angle of attack

Δx = PIV grid spacing [mm]

λ = Sparsity parameter

ν = Kinematic viscosity [m^2/s]

ϕ_k = Spatial POD mode

ψ_k = Temporal POD mode

ρ = Density [kg/m^3]

$\rho(a_k)$ = Correlation of estimated POD coefficients

ρ_{k,k_0} = Normalized mode-to-mode cross correlation

σ_k = Singular value (POD)

ξ_k = Model phase lag

ω_i = Vorticity [1/s]

I. Introduction

Upon encountering an adverse pressure gradient the incoming boundary layer on the suction surface of an airfoil is unable to remain attached to the surface and separates. An inflection occurs in the local stream-wise surface-normal velocity profile and a region of reverse flow (fluid with a velocity component opposite to the free stream) develops [1, 2]. The precise conditions for when this occurs depends on a number of factors including airfoil geometry, Reynolds number $Re_c = U_\infty c/\nu$ (with U_∞ the free stream velocity, c the airfoil chord length, and ν the fluid kinematic viscosity), and external conditions. Generally, at low angles of attack α the separation is contained to a small laminar bubble near the leading edge. As the angle of attack increases the bubble elongates, a phenomenon known as thin-airfoil (TA) stall [3, 4]. If the adverse pressure gradient is sufficiently strong a massive separation is observed characterised by the development of an incipient free shear layer [4–7]. Such a separation is known as leading edge (LE) stall or deep stall. Alternatively, separation may instead arise at the trailing edge of the airfoil progressing in the upstream direction, known as trailing edge (TE) stall [8].

The dynamics, and onset, of stalled airfoils has been for a century the subject of extensive research due to the abrupt changes that occur aerodynamically [1, 9, 10]. These changes include unwanted variations in hydrodynamic forces [11] and the generation of excess far-field noise [12, 13]. The onset of, or transition into, separation in the context of turbulent flow is a complex non-linear process [14] that is sensitive to the airfoil geometry [15–17], external conditions [18, 19], surface properties [20, 21], and non-trivially impacted by hysteresis [22, 23].

The onset and mechanism of static stall is influenced by the geometry of the airfoil, the Reynolds number, and external conditions. For example, TE stall is more typically encountered by cambered profiles [3, 24], but also occurs for symmetric ones [25]. Brunner et al. [23] demonstrated a change from TE stall to LE stall for a symmetric NACA 0021 airfoil as the Reynolds number increased beyond $Re_c = 2 \times 10^6$. Zaman et al. [26] experimentally demonstrated TE stall for both a symmetric NACA 0012 and a cambered LRN(1)-1007 at Re_c of $O(10^5)$. At the onset of static stall, the spectral signatures for both airfoils were found to be similar. However, for a cambered Wortmann FX 63-137, the stall onset was abruptly LE with spectral characteristics that differed substantially from the other airfoils. The influence of the airfoil geometry is clearly not trivial. This is further complicated by external influences, for example Swalwell et al. [27] showed for a NACA 0021 that free stream turbulence influences stall behaviour, with LE stall at low turbulence intensity and TE stall when turbulence intensity was increased to 7%.

Stalled airfoils exhibit characteristic frequency phenomena that persist despite the chaotic presence of turbulence at moderate to high Reynolds numbers [28]. These frequencies depend on the angle of attack. At angles near peak lift, where the airfoil transitions into a stalled state, energetic low-frequency phenomena are observed [26] at a non-dimensional frequency $f^\star_\alpha = f \frac{c}{U_\infty} \sin\alpha$ (where f is the frequency in Hz and α the angle of attack) of $O(10^{-2})$. This frequency is known to be associated with non-linear separation and reattachment and has been observed numerically [29, 30], experimentally [26], and has been predicted via linear instability analysis [14]. Beyond the critical stall angle a dominant frequency at $f^\star_\alpha$ of $O(10^{-1})$ emerges related to flapping shear layers at the leading and trailing edges [31, 32]. Likeness to observations of the flow over inclined flat plates [33] and 2D cylinders [34] confirms this frequency is the signature of bluff body vortex shedding phenomena [35].

The presence of dominant frequencies in the flow motivates the application of data-driven methods such as the proper orthogonal decomposition [POD; 36, 37] to educe low-order coherent flow structures [38]. It is of great interest to detect such coherent flow structures in real time for flow control applications aimed at stall manipulation for drag reduction [39–41] or reducing noise [42]. To this end, the POD basis can further be leveraged to predict the state of the flow using sparse estimation techniques [see 43, and references therein]. For example, the vorticity field of a laminar 2D cylinder in cross flow can be predicted exceeding 90% accuracy with only seven flow probes [44]. In comparison the flow of a turbulent stalled airfoil, as in the present study, is significantly more challenging to estimate with limited probes [45]. In fact, turbulent flows in general are exceedingly difficult to estimate from limited sensors [46]. This difficulty is further increased when the probes are restricted to surfaces i.e. in real-world applications that usually cannot take information at arbitrary points in the domain.

Despite the inherent difficulty, several studies utilizing linear stochastic estimation [LSE 47] have demonstrated success in predicting the flow state from limited pressure sensors e.g. in turbulent cavity flows [48, 49]. An extension of LSE to predict POD coefficients, termed LSE-POD [50], has been shown as more robust than LSE alone particularly for reduced order reconstruction [40, 51, 52]. The flexibility of LSE-POD allows to compare low-order dynamics across stalled airfoils with different geometries or angles of attack; lending valuable insight. The manner in which dominant frequencies manifest in low-order features and the resulting consequences on stall state estimation remains an open area of research.

The focus of the present study is that of turbulent stalled airfoils at moderate Reynolds number. Motivated by the complex features of such a flow, the objectives of the current study are two fold:

1) Identify and model the time-varying flow features underlying the turbulence of symmetric and cambered airfoils in transient and deep stall.
2) Explore the low-order dynamics using a data-driven approach towards feasibility of stall estimation from limited pressure probes.

To this end experimental data has been collected using time-resolved particle image velocimetry (PIV) in a water flume facility for symmetric and cambered airfoils at various angles of attack. In addition, planar pressure reconstructions are utilised to generate pseudo-pressure probes on the suction surface. The experimental data collection and reduction is presented in section II. A reduced-order analysis of the data is presented in section III. Data-driven flow sensing from pressure probes is then explored in section IV, with discussion and conclusions drawn in section V.

II. Experimental Data Sets

A. Data acquisition and post-processing

Time-resolved particle image velocimetry (PIV) data was collected in the University of Southampton water flume facility, featuring a test section 6.75 m long, a span of 1.2 m and water depth of 0.5 m. The airfoil models of chord length c = 15 cm and span s_{tot} = 70 cm were fixed vertically in the center of the span of the flume immediately following the contraction into the test section. The portion of the span that was submerged was s = 48.3 cm. PIV imaging was performed in the stream-wise surface-normal (x-y) plane as illustrated in figure 1(a). An overhead carriage system was

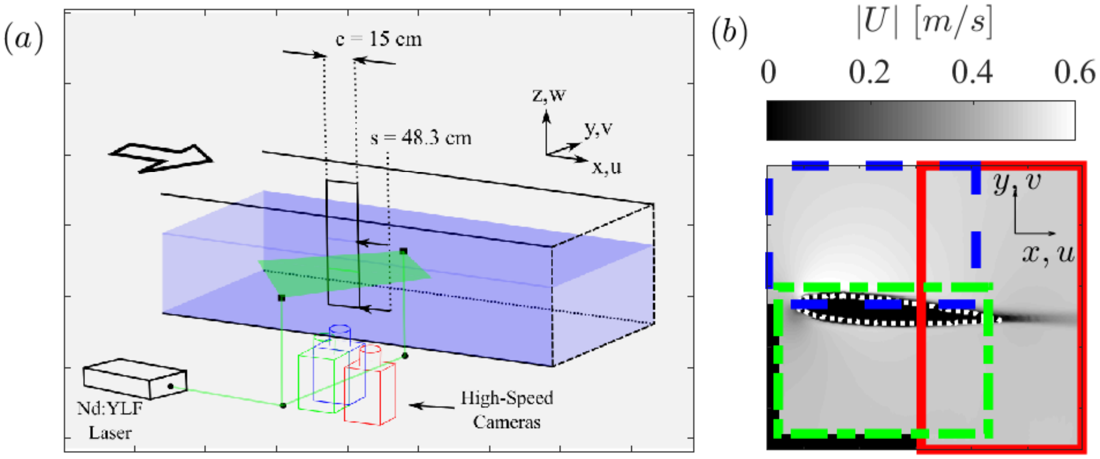

Fig. 1 Diagram (not to scale) of the experimental setup in the water channel facility to perform high-speed PIV (a). The pseudo-colour of velocity magnitude for the NACA 0012 at α = 4° is presented in (b) with the individual fields of view: - - - suction side, - - - pressure side, — trailing region and · · · indicates the nominal domain used for analysis.

employed to allow precise control of the angle of attack α. Angles of attack in the range $4° < \alpha < 17°$ at a chord-based Reynolds number $Re_c = \frac{U_\infty c}{\nu} \approx 7.1 \times 10^4$ (with U_∞ the free stream velocity, c the chord length, and ν the kinematic viscosity) were explored corresponding to a variety of stall conditions. An overview of the experimental cases is presented in table 1. The airfoil profiles and angles of attack were chosen to explore both the dynamics at peak lift as the foil transitions into stall and the dynamics post-stall. These dynamics are compared for a symmetric NACA 0012 and a cambered NACA 65-410 airfoil. The NACA 65-410 was chosen as it is designed to delay the onset of separation as relevant to turbine blades [53]. One additional case under attached flow conditions was obtained for the NACA 0012 for the purposes of measurement evaluation and validation.

A high-speed Nd:YLF laser (527 nm Litron) was directed inwards from either side of the facility to simultaneously illuminate the pressure, suction, and trailing regions of the airfoil and three 4 megapixel (2560 x 1600 pixels) high-speed Phantom Veo 640-S cameras mounting 105 mm Ex Sigma lenses (f# 5.6) were synchronized to capture the flow field surrounding the plane of the airfoil (figure 1b). Caution was exercised to ensure the laser sheets were aligned within the same plane, with an estimated sheet thickness of 2 mm at the location of the foil mid-chord. To compute the force quantities at each angle of attack, a six-axis force/torque load cell (ATI Delta IP65) was mounted to the airfoil and synchronized to the PIV acquisition using an NI USB-6251 DAQ. The free stream velocity was independently measured at the opposite end of the facility (beyond the wake recovery length generated by the foil) using a Hoentzsch FA flow meter situated in the mid-span of the flume.

The flow was seeded with Vestosint 2157 polyamide particles of nominal diameter 55 μm until a satisfactory seeding

Table 1 Parameters of experimental cases. The abbreviated dynamics refer to: A - Attached, TS - Transient Stall, DS - Deep Stall.

Profile	α°	C_L	Dynamics
NACA 0012	4	0.30	A
NACA 0012	13	0.51	TS
NACA 0012	15	0.49	DS
NACA 65-410	13	0.68	TS
NACA 65-410	15.5	0.64	DS
NACA 65-410	17	0.65	DS

density was obtained. Simultaneous high-speed images were collected across cameras at a frequency of 1 kHz and stored until memory limitations were reached, resulting in 5.367 seconds of continuous data. For each case, five such runs were repeated resulting in 26.84 seconds of data, corresponding to approximately 90 eddy turnover times $T = c/U_\infty$. The raw images of each camera were individually processed with background subtraction and Gaussian high-pass filtering with a filter width of 10 pixels to isolate the high-frequency particle reflections. Multi-pass planar PIV was performed using a verified in-house Matlab code with 3 passes per window size and square windows decreasing from 64 by 64 pixels, to 32 by 32 pixels, to 24 by 24 pixels with 50% overlap. The final vector spacing was $\Delta x = 0.83$ mm corresponding to 181 vectors spanning the airfoil chord. PIV outliers were replaced using robust principle component analysis [54] with the sparsity parameter at the theoretical optimum of $\lambda = 1$ and the inexact augmented lagrangian method for iteration [55, 56]. Based on sub-pixel accuracy down to 0.05 pixels, the bias uncertainty of the stitched PIV is approximately 2.5 mm/s (or 0.5% of the free stream velocity).

Prior to each measurement case, a calibration image spanning all three cameras was collected using a target aligned with the laser sheet plane. This was used to correct distortions [57] and calibrate the PIV fields. The overlap across the fields of view within the calibration images was used for reference positions to stitch the velocity fields together [58]. The stitching was performed on the calibrated vector fields using a Hamming window for blending. To account for the unequal PIV grid sizes, the PIV vectors of the highest resolution grids (the suction and pressure fields of view) were bi-linearly interpolated to the lowest resolution grid (the trailing field of view) to avoid spatial up-sampling during stitching. Due to the airfoil extending downwards in the direction of the upward-facing cameras, a visual occlusion was produced on the pressure side of the airfoil, preventing from measuring the flow close to the surface. In addition to the foil cross section, the occluded region was masked in the final vector fields. Surface profiles on the pressure side reported hereafter are linearly interpolated to the foil surface using the nearest available data points. The final PIV fields were spatially truncated along the edges to form a rectangular domain (figure 1b). To avoid some high frequency artifacts detected *a-posteriori*, all forces and velocity fields were temporally filtered to 10 Hz using a Gaussian low-pass filter. This limits the scope of the temporal analysis of the present work to frequencies below a non-dimensional frequency

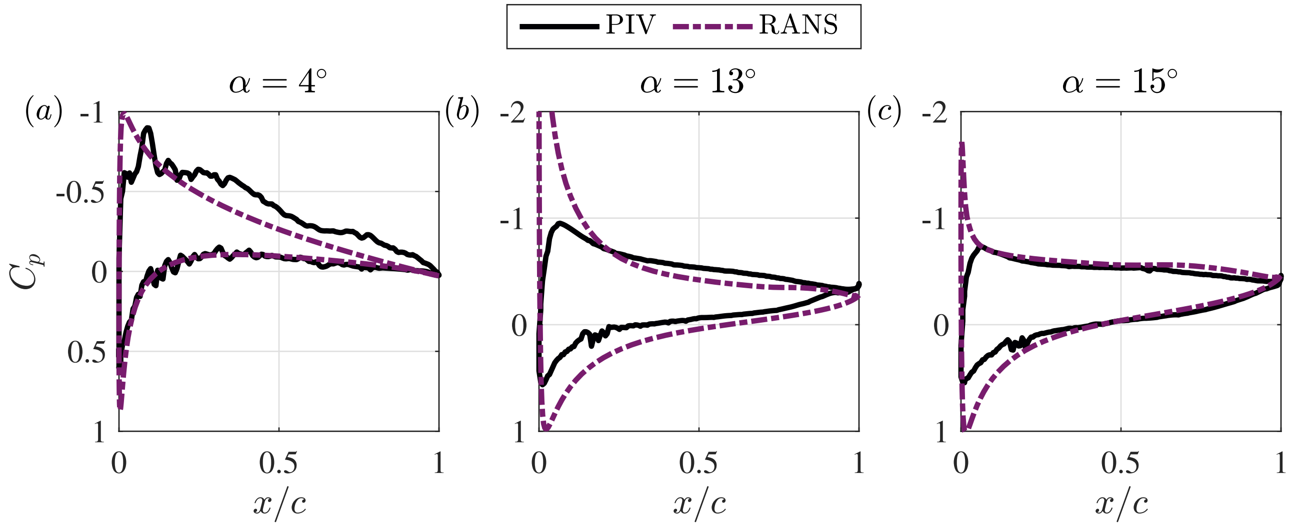

Fig. 2 Mean reconstructed surface pressure coefficient profiles for the NACA 0012 cases from the planar PIV at α = 4° (a), α = 13° (b) and α = 15° (c). The PIV data (—) is compared to a dynamically matched RANS (- - -).

$f^\star = f \frac{c}{U_\infty} \leq 3$.

B. Planar pressure reconstruction

Planar pressure fields were reconstructed from the instantaneous velocity fields using a Poisson solver approach [59–61]. Neumann boundary conditions were applied on the inlet, outlet, and suction (upper) boundaries of the domain and Dirichlet boundary conditions were employed using Bernoulli's equation in the free stream on the pressure (lower) domain boundary, where the flow is most approximately irrotational. Due to the presence of reverse flow in stalled cases, Taylor's hypothesis was not invoked to estimate the unsteady velocity term $\partial u_i / \partial t$ [where u_i is the instantaneous flow field and t the time, 60]. Instead, the unsteady velocity term was directly computed from the highly time-resolved Eulerian fields [62]. Good agreement using central temporal differences up to sixth order was found, therefore second order gradients were opted for in favor of processing speed. Spatial derivatives were computed using second-order central differences.

To provide comparison for the mean pressure fields computed from planar PIV, an unsteady two-dimensional Reynolds-averaged Navier-Stokes (RANS) simulation was performed for the NACA 0012 cases using OpenFOAM software. The simulation utilized a k-ω shear stress transport (SST) closure model. A standard C-type domain and grid geometry was chosen with a horizontal and vertical extent of 20 chords lengths. The simulation properties (e.g. kinematic viscosity, inlet velocity, chord length) were chosen to match identically those of the experiment. The comparison between the pressure coefficient along the foil surface $C_p = P / \frac{1}{2} \rho U_\infty^2$ (with P the mean pressure field and ρ the density) in the PIV and RANS is shown in Figure 2.

The agreement in the attached case (figure 2a) is found to be satisfactory, though not without difficulty. The PIV was unable to capture the suction peak near the leading edge and overestimated the magnitude of the pressure along the suction side. Difficulty in capturing this suction peak has been identified in previous studies [63–65]. At higher angles of attack (figure 2b,c), despite good qualitative agreement, the PIV was found to significantly underestimate the magnitude of the suction peak. However, the surface pressure on the suction side at $x/c > 0.1$ recovers reasonably closely to the RANS. Accounting for the limited size of the PIV domain, the time-averaged surface pressure distributions are deemed to satisfactory, and lend confidence to the approximation of the planar reconstruction.

C. Basic statistical field quantities

Following the PIV post-processing, the basic flow statistics for each case were obtained. The velocity and pressure fields were decomposed into mean and fluctuating components $u_i(\boldsymbol{x}, t) = U_i(\boldsymbol{x}) + u_i'(\boldsymbol{x}, t)$ and $p(\boldsymbol{x}, t) = P(\boldsymbol{x}) + p'(\boldsymbol{x}, t)$ where capitalised variables denote the mean and the prime symbol the fluctuating components. The explicit space and time dependence of field variables are implied and hereafter omitted. The planar turbulent kinetic energy is defined as TKE= $\frac{1}{2}(u_{rms}^2 + v_{rms}^2)$ where u_{rms} and v_{rms} are the root-mean-square freestream and stream-normal velocity fluctuations, respectively. These fields are presented in figures 3 and 4 for the NACA 0012 and NACA 65-410, respectively. They capture the basic physical description of the various cases.

Starting with the NACA 0012 cases (figure 3) at $\alpha = 4°$, the mean velocity field indicates the flow is attached as expected. A negative pressure region is seen on the suction side and a positive region on the pressure side proximal to the leading edge. At $\alpha = 13°$, the mean velocity field indicates clear separation as evidenced by the region of flow reversal [66] near the foil surface on the suction side ($u < 0$, see the dash-dot white contour of the figure). A wide region of significant TKE develops in a shear layer on the suction side. Similar observations hold for the $\alpha = 15°$ case, but with a larger region of reverse flow and a comparatively elevated shear layer. A more stringent indication of deep stall can be deduced from the pressure on the suction side, for which the surface pressure gradient along the surface is expected to go to zero. In other words, for stalled conditions, the mean pressure along the separated region of the surface is expected to be constant. This is most evident for the $\alpha = 15°$ case (see figure 2), whereas the $\alpha = 13°$ case sees a non-zero decrease in pressure in this region. This small but non-zero decrease is likely due to non-linear reattachment near the leading edge associated to transient stall [8, 14]. During time periods of reattachment, the flow experiences a non-zero local pressure gradient and this biases the distribution in the overall mean surface pressure profile to have a small, but non-zero, slope [in agreement with e.g. 30].

The basic statistical field quantities of the cambered NACA 65-410 show similar qualitative behavior to the stalled NACA 0012 cases (figure 4). At $\alpha = 13°$, the region of reverse flow is confined to a relatively thin layer near the surface. This confirms the performance of the cambered profile to reduce separation at the same angle of attack compared to the symmetric one. The pressure gradient appears to monotonically decrease along the foil surface (figure 4c), suggesting a state of transient stall similar to the NACA 0012 at $\alpha = 13°$. As the angle of attack increases across cases to $\alpha = 15.5°$

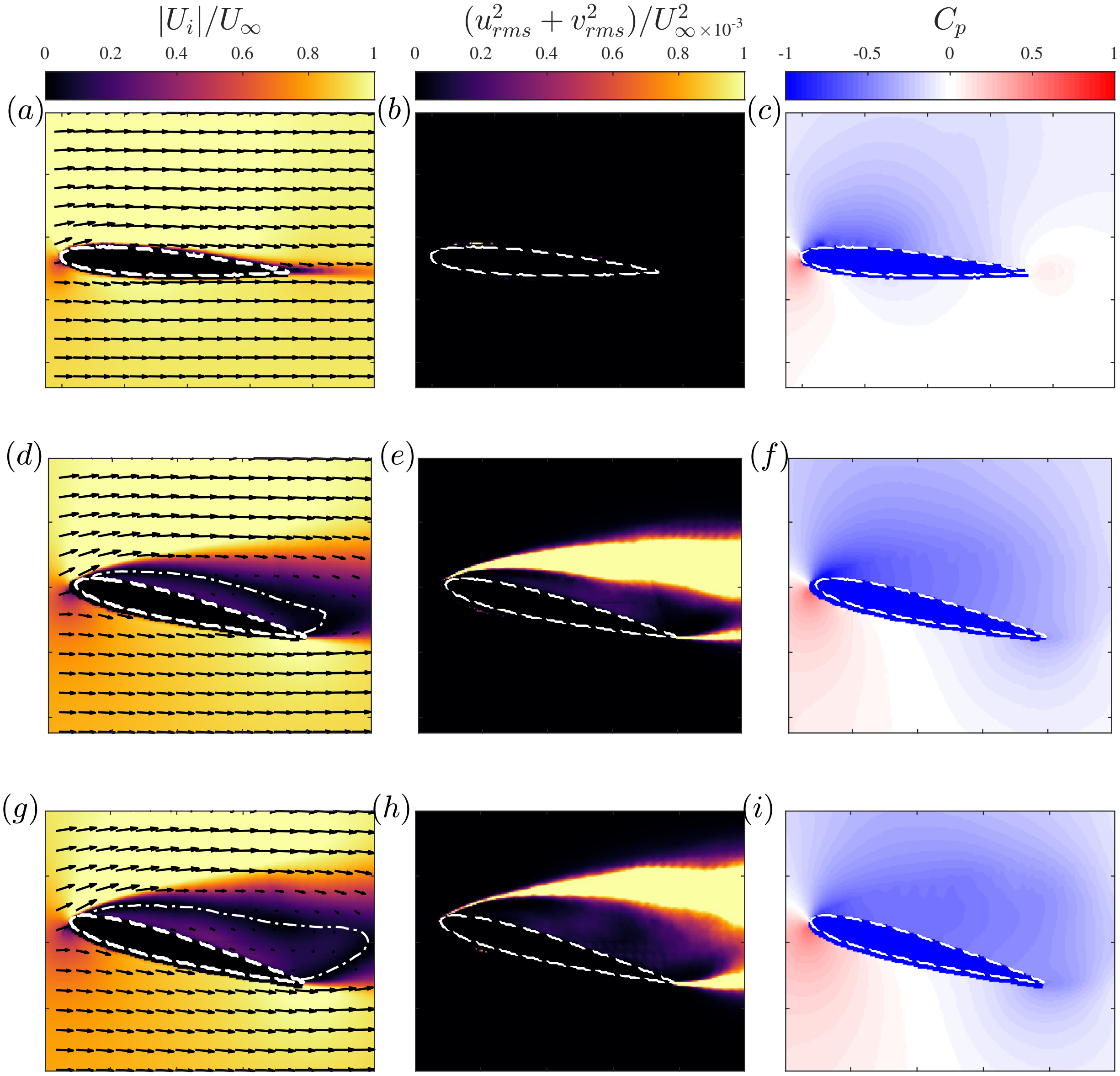

Fig. 3 **Mean velocity fields (a,d,g), planar turbulent kinetic energy fields (b,e,h), and mean pressure coefficient fields (c,f,i) for the NACA 0012 cases at $\alpha = 4°$ (a-c), $\alpha = 13°$ (d-f) and $\alpha = 15°$ (g-i). The mean velocity has every fifteenth vector shown and the white dash-dot contour corresponds to $u = 0$. Within the contour, the flow is seen to move opposite the freestream.**

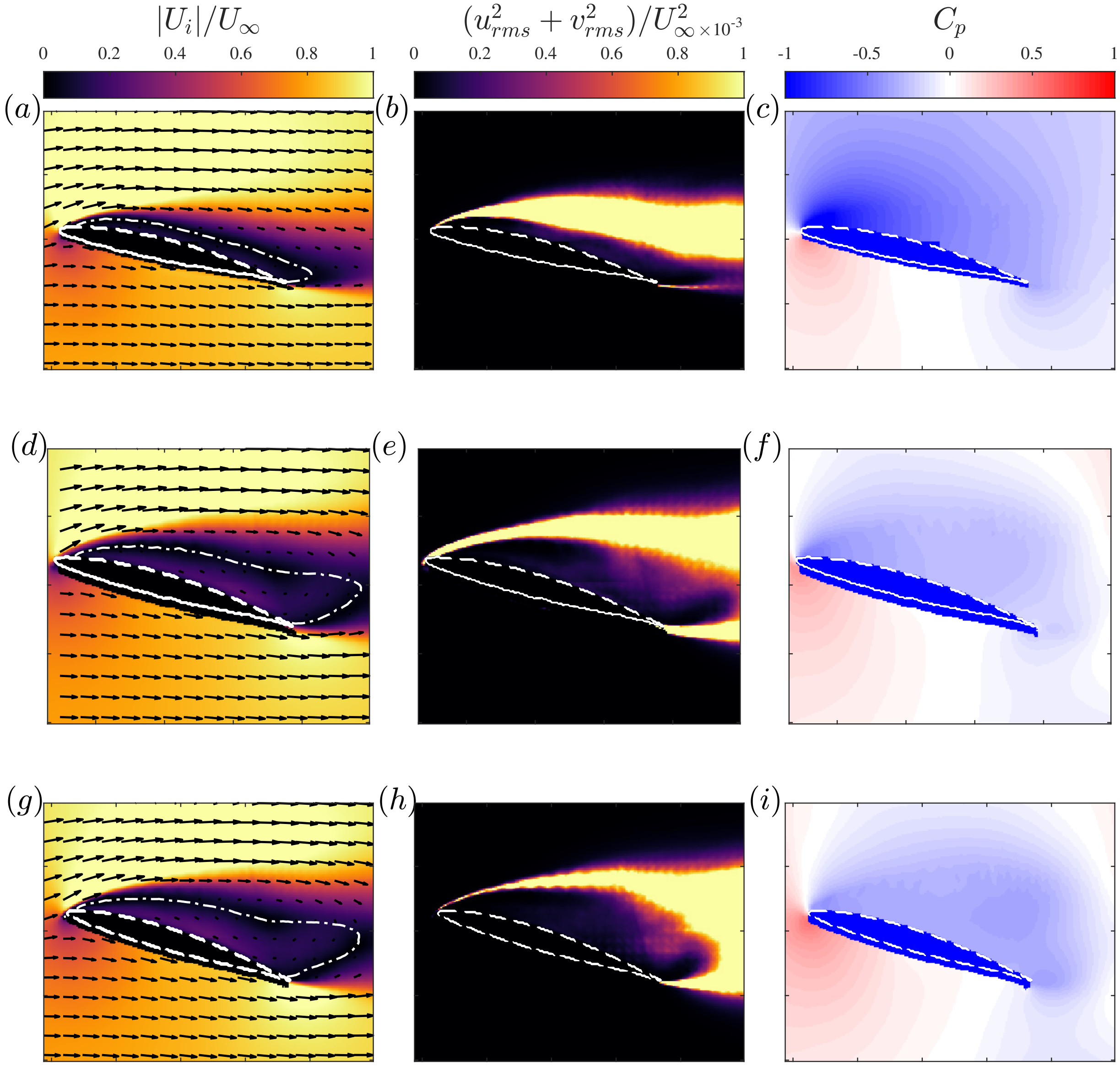

Fig. 4 Mean velocity fields (a,d,g), planar turbulent kinetic energy fields (b,e,h), and mean pressure fields (c,f,i) for the NACA 65-410 cases at $\alpha = 13°$ (a-c), $\alpha = 15.5°$ (d-f) and $\alpha = 17°$ (g-i). The mean velocity has every fifteenth vector shown and the white dash-dot contour corresponds to $u = 0$. Within the contour, the flow is seen to move opposite the freestream.

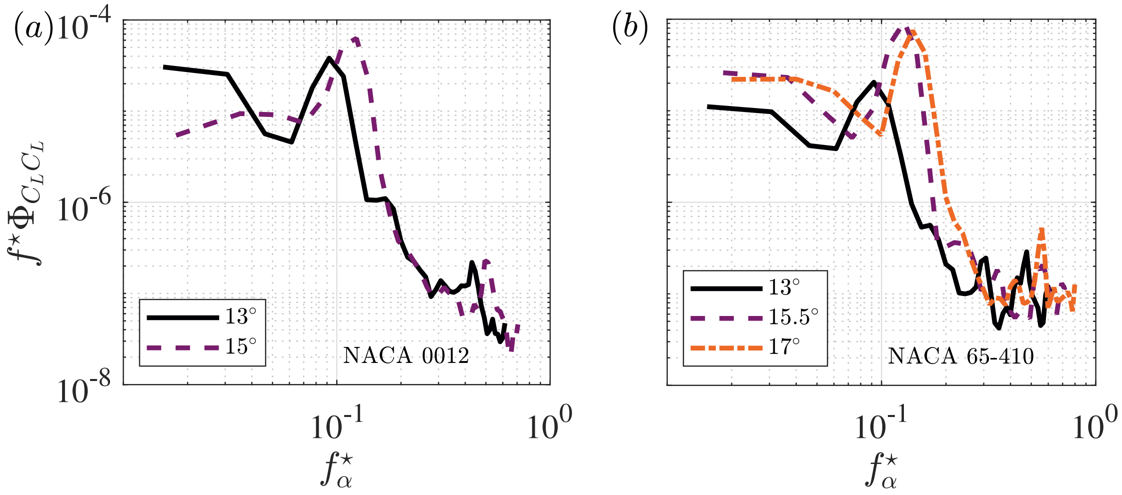

Fig. 5 Premultiplied lift coefficient power spectral densities $\Phi_{C_L C_L}$ for the NACA 0012 (a) and NACA 65-410 (b) cases.

and $\alpha = 17°$, deep stall is reflected by the significant region of flow reversal, an elevated shear layer and a constant surface pressure profile on the suction side. These observations of stall state are used to characterize the various cases in table 1 as either in transient stall (TS) or deep stall (DS).

Across all stalled cases, the significant TKE in the shear layer as well as a negative pressure on the suction side gives confidence to the fidelity of the PIV measurements. There is however a small-scale bias error evident from the second-order statistics, i.e. the fringe-like patterns in the TKE pseudo-color profiles of figures 3 and 4. This is likely not related to the PIV stitching, but rather may be caused by a slight misalignment between the overlapping planar laser sheets. This small-scale bias may propagate error into gradient-based quantities such as the pressure and the (out-of-plane) vorticity defined as the curl of the velocity field $\boldsymbol{\omega} = \boldsymbol{\nabla} \times \boldsymbol{u}$. For the pressure, this is not of significant concern due to the property of the Poisson solver effectively acting as a low-pass filter [59]. For the vorticity, this is addressed employing a Gaussian low-pass filter with a width of 5 vectors, or 4 mm, to the velocity fields before computing the gradients. The filter width corresponds to approximately twice the thickness of a single laser sheet, thereby accounting for generous misalignment. The magnitude of the out-of-plane vorticity due to the application of the filter was found to differ by approximately 10%.

The time-varying flow behaviour is most readily characterised upon inspection of the lift coefficient spectra calculated from the simultaneous load cell data presented in figure 5. The instantaneous sectional lift coefficient was calculated as $C_L(t) = L(t)/\frac{1}{2}\rho U_\infty^2 cs$ where $L(t)$ is the instantaneous lift measurement in Newtons from the load cell. A peak corresponding to bluff-body shedding phenomena is evident in all cases at a non-dimensional frequency based on the cross-stream projected chord $f_\alpha^\star = f\frac{c}{U_\infty \sin\alpha} \approx 0.15$ [35]. The TS cases have accompanying, albeit broad, low frequency peaks of at $f_\alpha^\star$ of O(10^{-2}). This peak is higher relative to the the bluff-body peak in comparison with the DS cases. The spectral behaviour confirms the characterization of the stall regimes from the qualitative inspection of the mean velocity and pressure fields. The underlying mechanism most likely responsible for the low-frequencies will be discussed further in section III. A rightward shift in the peak of $f^{\star}_{\alpha}$ with increasing angle of attack is also evident.

III. Low-order analysis

In this section a data-driven approach is used to separate the underlying flow coherence from the broad-spectrum turbulent fluctuations. The application of such an approach to model the low-order dynamics as well as to establish a basis for state estimation via limited probes is explored.

A. Application of the proper orthogonal decomposition

To investigate the structures underlying the turbulence, the data-driven proper orthogonal decomposition [POD, 37] is invoked. For the present time-resolved PIV data, POD allows to decompose the fluctuating velocity and pressure fields into the sum of the product of time-varying coefficients $a_k(t)$ with time-invariant orthogonal spatial modes $\boldsymbol{\phi}_k(\boldsymbol{x})$, e.g. for the pressure

$$p'(\boldsymbol{x},t) = \sum_{k=1}^{N} a_k^p(t)\boldsymbol{\phi}_k^p(\boldsymbol{x}) \tag{1}$$

where k is the mode number, N is the total number of modes, and the superscript notation here corresponds to the quantity of interest (either p for pressure or uv for velocity). The spatial modes are determined via the eigendecomposition of the cross-correlation tensor for the quantity of interest [see e.g. 37, 38, 67]. The coefficients can alternatively be expressed as $a_k(t) = \psi_k(t)\sigma_k$, where $\psi_k(t)$ is orthogonal in time and referred to as the temporal mode and σ_k is the (time-independent) k-th singular value characterising the magnitude of each coefficient and the relative contribution of each spatial mode. By convention, the modes are placed in descending order of the singular values.

Due to the large data sets in the present study, the global spatial basis and singular value distributions were tabulated sub-sampling one in every 25 snapshots for a total number of snapshots $N = 1075$ for each case. The instantaneous coefficients were then obtained for each run through a projection of the field variables onto the spatial basis. The coefficients were re-scaled using the respective singular values (i.e. $\psi_k(t) = a_k(t)/\sigma_k$) to calculate the spectra of the temporal modes.

The pre-multiplied spectra of the temporal modes for the NACA 65-410 in TS at $\alpha = 13°$ and DS at $\alpha = 17°$ are shown in figure 6(b-e). These results are found to be representative of all other TS and DS cases that are omitted for brevity. Distinct spectral peaks can be seen for both the velocity and pressure modes. As the mode number increases the spectrum peak eventually shifts to higher frequencies, likely due to bluff body shedding and shear layer flapping [12]. In addition, the distribution broadens, pointing to the association of the higher modes with broad-spectrum turbulence. For the DS case at $\alpha = 17°$, a clear peak is seen in the first three modes at the shedding frequency observed in the lift spectra

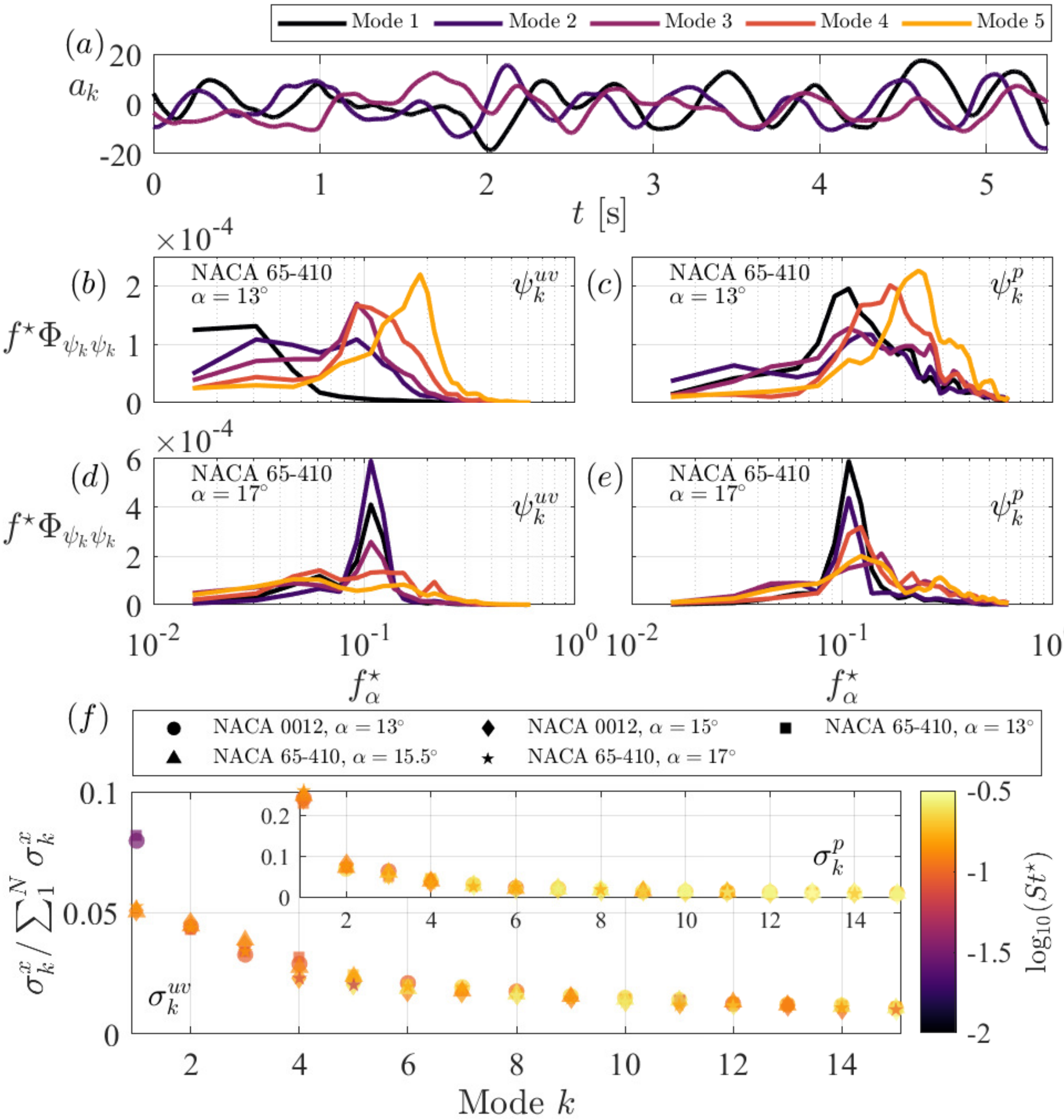

Fig. 6 **Example POD coefficients for one run of the DS case of the NACA 65-410 at $\alpha = 17^\circ$ (a). Pre-multiplied spectra of the first five temporal velocity (b,d) and pressure (c,e) modes for the NACA 65-410 in TS at $\alpha = 13^\circ$ (b,c) and DS at $\alpha = 17^\circ$ (d,e). The first fifteen singular values (normalised by the total sum) are shown in (f), coloured by the logarithm of the peak Strouhal number in the spectrum of each velocity mode (outset) and pressure mode (inset).**

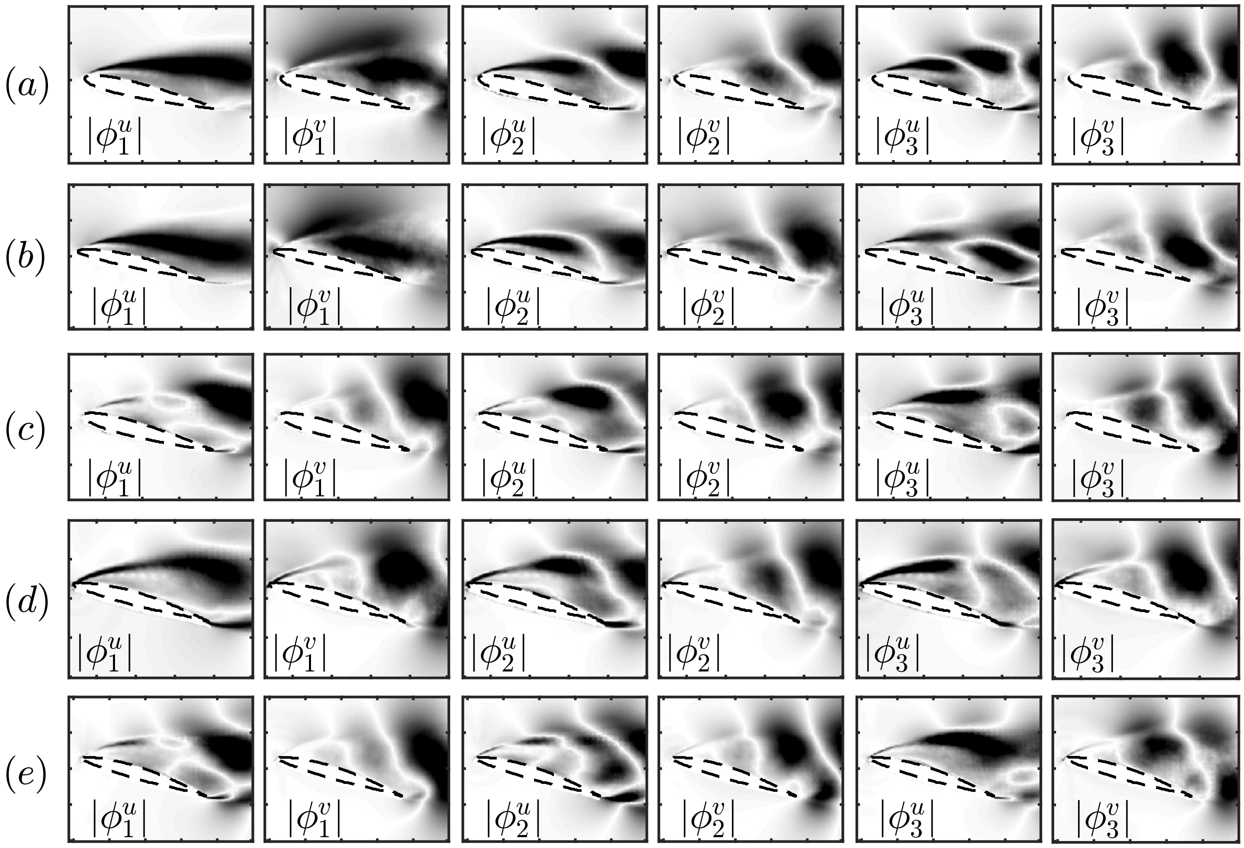

Fig. 7 First three spatial velocity mode magnitudes for the stream-wise and stream-normal components ϕ_k^u and ϕ_k^v for the TS cases of NACA 0012 and NACA 65-410 at $\alpha = 13°$ (a,b) and DS cases of NACA 0012 at $\alpha = 15°$ (c) and NACA 65-410 at $\alpha = 15.5°, 17°$ (d,e). White to black colours correspond to 0 to 3 standard deviations of each mode.

of section II.C. For the TS case at $\alpha = 13°$, the first velocity mode peaks at $f_\alpha^\star \approx 0.03$ and the peak shifts to higher values gradually. The comparison between TS and DS spectra contrast the range of distinct frequencies in the low-order modes. The TS cases exhibit a range of peaks, whereas the low-order features of the DS cases are primarily rooted in bluff-body shedding phenomena.

To exemplify the peak frequency associated to each mode across cases, a Strouhal number $St^\star$ is defined as the frequency $f_\alpha^\star$ for which the spectrum of each velocity mode is maximum. The singular values for each run, coloured by $\log_{10}(St^\star)$, is shown in figure 6(f). This highlights the low-frequency peak associated to the first mode in the TS cases. Not only is the frequency low, but the contribution to the root mean-square fluctuation is 50% higher than the first mode of the DS cases. This points to significant energy in the low-frequency phenomena of the TS cases.

For insight on the low-order spatial structures, the first three spatial modes of the velocity are presented for all cases in figure 7. It should be noted as a general property of POD that the sign (positive or negative) of the spatial modes is arbitrary between cases, thus the figure presents the magnitude of the modes. The mode shapes reveal the nature of the

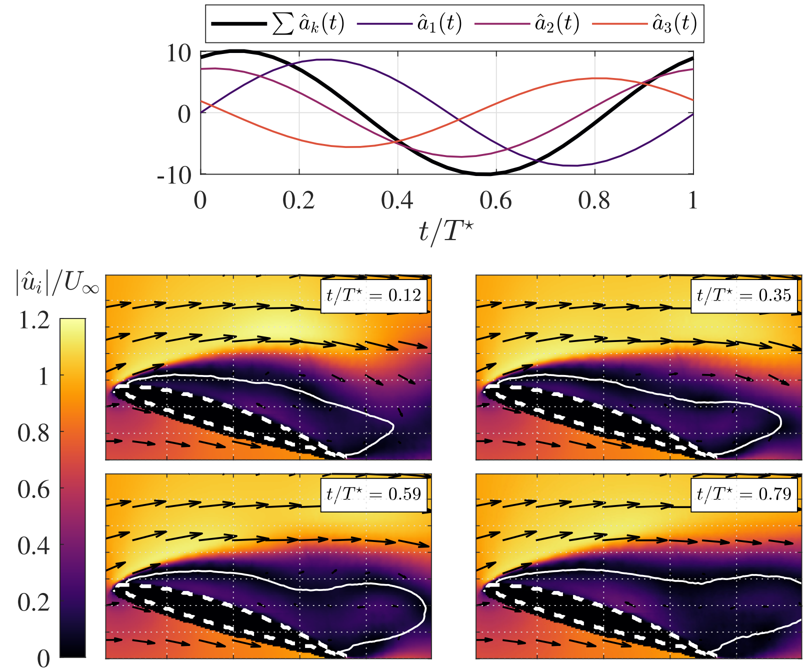

Fig. 8 Synthetic model for the NACA 65-410 at $\alpha = 17°$ in DS. The sinusoidal coefficients (upper) are used to drive the reconstruction (lower), shown zoomed in on the suction region at four instants over the model cycle. The white contour highlights the region of reverse flow ($u < 0$) corresponding to separation. One in 25 vectors are shown.

TS low frequency oscillations at $f^{\star}_{\alpha}$ of $O(10^{-2})$. The structures in both u and v are nearly uniform across the suction side; acting as a large-scale physical envelope. This envelope modulates the flow fields over long time scales, pushing and pulling the region of reverse flow ($u < 0$) in a direction normal to the suction surface. The interpretation of the associated spectral peak is complicated somewhat by the resolution of such low-frequencies. The apparently broad peak may be due to limited convergence, but may also be the manifestation of the separation and reattachment phenomena occurring intermittently on long time scales [14]. However, some results using long time series at a single point suggest such a peak is pronounced in reality [26], indicating that this mode may be fluctuating at a fixed frequency.

Such a large structure is not seen for the DS cases. Instead, the DS cases feature alternating positive/negative regions at the leading and trailing edges in the first mode. This reflects the alternating shedding at the characteristic frequency $f^{\star}_{\alpha} \approx 0.15$ in these cases. This is consistent with the spectra of the temporal coefficients (figure 6).

There is a striking resemblance in the structure of the spatial modes across cases within the same flow regime (either TS or DS) despite the difference in the airfoil geometries. This lends support towards the notion that the low-order dynamics may not be sensitive to the exact shape or symmetry of the foil surface. The implications of such low-order similarity are further explored in section IV.

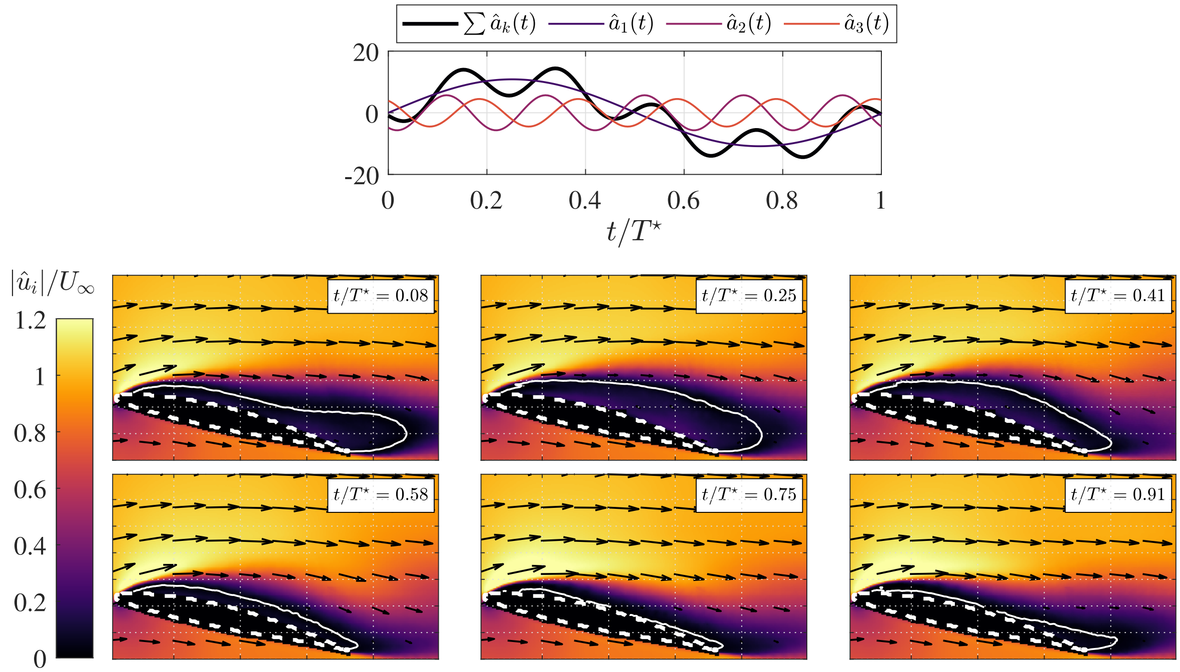

Fig. 9 Synthetic model for the NACA 65-410 at $\alpha = 13°$ in TS. The sinusoidal coefficients (upper) are used to drive the reconstruction (lower), shown zoomed in on the suction region at six instants over the model cycle. The white contour highlights the region of reverse flow ($u < 0$) corresponding to separation. One in 25 vectors are shown.

B. Model dynamics using three modes

Motivated by distinct peak frequencies associated to each mode (figure 6), in this section the POD basis is leveraged to gain insight on the low-order dynamics. A simplified model is constructed for each airfoil using the superposition of sine waves at the frequency defined by the Strouhal number $St^\star$ of the low-order modes. The number of chosen modes is a trade off between retaining as much energy of the fluctuating fields as possible whilst retaining only the modes with distinct peaks that underlay the broad-spectrum turbulence. Based on the prominence of the spectral peaks, we select the first three modes in each case (figure 7) to construct the model. In the model, the k-th model coefficient $\hat{a}_k^{uv}$ is approximated as

$$\hat{a}_k^{uv}(t) = A_k \sin(2\pi f_k^{St^\star} t + \xi_k) \tag{2}$$

where the amplitude $A_k = \sigma_k/\sqrt{N}$, $f_k^{St^\star} = St^\star \frac{U_\infty}{c \sin\alpha}$ is the k-th Strouhal frequency in seconds, and the phase is obtained as $\xi_k = 2\pi f_{k_0}^{St^\star} \Delta t_{k_0,k}$ with the choice $k_0 = 1$. The phase lag $\Delta t_{k_0,k}$ is the time delay between the reference mode k_0 and k-th mode, obtained via the maximum of the magnitude of the averaged cross correlation $\rho_{k_0,k}(\Delta t)$ between the POD coefficients, where Δt is a time lag. The maximum of the cross correlation between modes was found to vary depending on the case from $\rho_{k_0,k} \approx 0.4$ to 0.9, indicating that a consistent phase difference between the modes is a reasonable approximation for the simplified model. The time domain is selected to vary over a period $T^\star = 1/St^\star_{min}$ corresponding to the lowest Strouhal frequency of the three modes in the model. The model reconstruction is then obtained via

$$\hat{\boldsymbol{u}}(\boldsymbol{x}, t) = \sum_{k=1}^{3} \hat{a}_k^{uv}(t)\boldsymbol{\phi}_k^{uv}(\boldsymbol{x}) + \boldsymbol{U}(\boldsymbol{x}). \tag{3}$$

Animations of the model reconstructions are provided in the supplementary material for representative DS and TS cases (figure S1 and figure S2, respectively). A model reconstruction is presented for a representative DS case in figure 8 for the NACA 65-410 at $\alpha = 17°$. The Strouhal number $St^\star$ is found to be the same for the first three coefficients, resulting in a model with a simple overall sine wave variation at one frequency. A likeness between the variation in the model and the real coefficients can be seen by comparison to figure 6(a). The white contour at $u = 0$ reveals the region of reverse flow elongates at the trailing edge at $t/T^\star = 0.79$, before returning proximal to the suction surface by $t/T^\star = 0.12$. This reflects the effect of the bluff body shedding on the region of reverse flow. At the leading edge, the reverse flow contour is seen to oscillate in the vertical direction corresponding to the incipient shear layer flapping. This phenomenon, consistent with observations of the raw velocity fields, is seen to occur simultaneously at the leading and trailing edges. As the model is based on one single frequency, this reaffirms the phase locked relationship between the incipient shear layer flapping and trailing edge shedding.

The model for the TS cases reflects the comparatively complex low-order dynamics in figure 9 for the representative case of the NACA 65-410 at $\alpha = 13°$. The model reveals the overall role played by the low-frequency phenomenon at $f^\star_\alpha \approx 0.03$. When the coefficient $\hat{a}_1$ reaches its maximum, the separated region is also maximal ($t/T^\star = 0.25$). At its minimum, the flow is seen to reattach ($t/T^\star = 0.75$). Further, the growth of the separated region appears to originate at the trailing edge ($t/T^\star = 0.91$), possibly indicative of trailing edge stall [8]. The sinusoidal variation of the separated region appears to oscillate along the chord, similar to the laminar separation bubble elongating and bursting as identified numerically by ElAwad and ElJack [29] at similar $f^\star_\alpha$. The high-energy low-frequency expansion and contraction of the separated region explains the comparatively wide region of TKE (figures 3 and 4) in the TS cases compared to the thin region of TKE concentrated at the incipient shear layer for the DS cases.

The model reveals important underlying dynamics of the flow fields. However, it is important to emphasize its low-order and simplified nature. It is based on a single frequency per mode, a single phase-difference (between each mode), and only three total modes. Three modes corresponds to only 15-20% of the total magnitude of the turbulent kinetic energy (figure 6). The remaining energy is attributed to the increasingly broad spectrum and fine-scale features of the remaining modes.

IV. Flow state estimation from surface pressure probes

The similar spatial structure and spectral content of the modes across either the TS or DS cases suggests the low-order dynamics in the POD basis may be robust across airfoil geometries. This has important implications for example in sparse reconstructions [44], where the state of the flow is estimated from limited probes or sensors [45, 68]. As the present data set contains simultaneous velocity and (reconstructed) pressure measurements, the pressure at the suction surface will be utilized as pseudo probes to determine the low-order state of the velocity field. In the following the efficacy of such a determination is quantified from the present data set. Ideally, it would be best to use a limited amount of sensors to predict the state of the flow. Given that the POD analysis indicates that three modes capture the dynamics of the flow, three different pressure probes are used in order to estimate the POD coefficients.

A. Low-order LSE-POD reconstruction via pseudo-pressure probes

Three pseudo-pressure probes are placed on the surface of the airfoils at the leading edge, mid-chord, and trailing edge ($x/c = 0, 0.5, 1$) and utilized to estimate the low-order state of the velocity fields from three POD modes. To this end linear stochastic estimation (LSE) is employed [47, 69]. LSE has been demonstrated to accurately predict the state of turbulent flow from limited flow sensors [70] or a related measurement such as pressure sensors e.g. in cavity flows [48, 49]. The concept of LSE has since been adapted in a hybrid approach [50, 52] termed LSE-POD for which the LSE is used to estimate the POD coefficients. The hybrid approach is adopted in the present study to estimate the low-order state of the velocity field, and in particular the location of the separated region. In the following the application of LSE-POD to the reconstruction of the first three modes from surface pressure signals is presented. For more on the technique the interested reader is referred to e.g. Murray and Ukeiley [48], Tinney et al. [71], and Lasagna et al. [49]. As LSE-POD is an established method, the details on the present implementation may be found in Appendix A.

Three metrics are utilised to assess the LSE-POD reconstructions. The correlation of the estimated coefficients is defined as

$$\rho(a_k) = \frac{\langle a_k^*(t) a_k(t) \rangle}{\sigma_{a_k^*} \sigma_{a_k}} \tag{4}$$

where $\sigma_{a_k^*}$ and σ_{a_k} are the standard deviations of the k-th estimated (a_k^*) and real (a_k) POD coefficient such that 1, 0, and -1 corresponds to perfectly correlated, uncorrelated, and anti-correlated coefficients. The angled brackets denote averaging over all time steps in the testing data. The error of the estimated coefficients is defined as

$$e(a_k) = \frac{\langle |a_k^*(t) - a_k(t)| \rangle}{\sigma_{a_k}} \tag{5}$$

such that $e = 0$ corresponds to a perfect reconstruction and $e = 1$ corresponds to the average error equal to σ_{a_k} (a situation that occurs e.g. when $a_k^* \to 0$) and $e > 1$ denotes inaccuracy exceeding the standard deviation of the coefficient.

An additional error metric is defined for quantifying the accuracy of the reconstruction of the separated region

$$e_c = \frac{\left\langle \sqrt{\left(\overline{x^*}(t) - \overline{x}(t)\right)^2 - \left(\overline{y^*}(t) - \overline{y}(t)\right)^2}\, \right\rangle}{c} \tag{6}$$

where $(\overline{x}(t), \overline{y}(t))$ and $(\overline{x^*}(t), \overline{y^*}(t))$ are the coordinates of the instantaneous centroid of the separated region ($u < 0$) in the three-mode POD reconstruction and LSE-POD reconstruction, respectively. When $e_c = 0$, the centroid position of the separated region is perfectly estimated and $e_c = 1$ corresponds to an average imprecision on the location of the centroid by the chord length of the foil.

To thoroughly assess the accuracy of the LSE-POD method five permutations of training and testing data are used and assessed using equations 4-6. For example, we use runs one through four to train the LSE coefficients and test on run five. We then permute and use runs one through three and five to train the LSE coefficients and test on run four, etc. The overall correlation and error is obtained as the average from all five possible permutations of training and testing data.

The overall correlation and error are presented in figure 10 (filled symbols) for the three mode coefficients (a-c) and the centroid error in the separated region of the low-order reconstruction in (d). The correlation (filled black squares) varies depending on the case, but is generally non-zero and positive. The highest correlations are found for a_2 and a_3 with a maximum correlation $\rho_{max} = 0.80 \pm 0.04$ and minimum error $e_{min} = 0.61 \pm 0.06$ in a_2 for the NACA 65-410 at $\alpha = 17^\circ$. This case is shown for one run in figure 11(e). In general, reconstructions with a high correlation (i.e. $\rho > 0.5$) correspond to low error ($e < 1$). Conversely, poor correlations results in excessive error. It can be seen upon inspection of figure 11, errors at $e \approx 1$ are generally caused by underestimation in the magnitude of the instantaneous coefficient (as opposed to wild inaccuracies).

The location of the low-order centroid is found to be accurate to within 10% of the chord with the exception of the NACA 65-410 at $\alpha = 13^\circ$. Close inspection of this case revealed that the increased centroid error is due to low-probability instances in which reverse flow extends downstream and the centroid locates near the trailing edge. The reconstruction places it near the leading edge, resulting in centroid error as high as 90% of the chord. These infrequent instances bias the mean towards an average centroid error close to 25%.

B. xLSE: Application of LSE coefficients across airfoil geometries

Motivated by the similar spectral content and spatial structures across the first three modes between the TS cases and DS cases separately, a cross-LSE (xLSE) approach is taken. For this approach, the LSE coefficients from one airfoil geometry are applied to the instantaneous pressure probes for a different geometry to obtain an estimate for the state of the flow. An overview of xLSE test cases is given in table 2. The instantaneous POD coefficients are obtain as

$$a_k^x(t) = P_i(t)\tilde{B}_{ij}S_{jk} \tag{7}$$

Table 2 Table of xLSE cases indicating the data used to generate the LSE coefficients (LSE library) and the data for which the coefficients are used with the probe signals to test the reconstruction (testing data).

Case ID	LSE Library	Testing Data
TS1	NACA 0012, $\alpha = 13°$	NACA 65-410, $\alpha = 13°$
TS2	NACA 65-410, $\alpha = 13°$	NACA 0012, $\alpha = 13°$
DS1	NACA 0012, $\alpha = 15°$	NACA 65-410, $\alpha = 15.5°$
DS2a	NACA 65-410, $\alpha = 15.5°$	NACA 0012, $\alpha = 15°$
DS2b	NACA 65-410, $\alpha = 17°$	NACA 0012, $\alpha = 15°$
DS3	NACA 0012, $\alpha = 15°$	NACA 65-410, $\alpha = 17°$

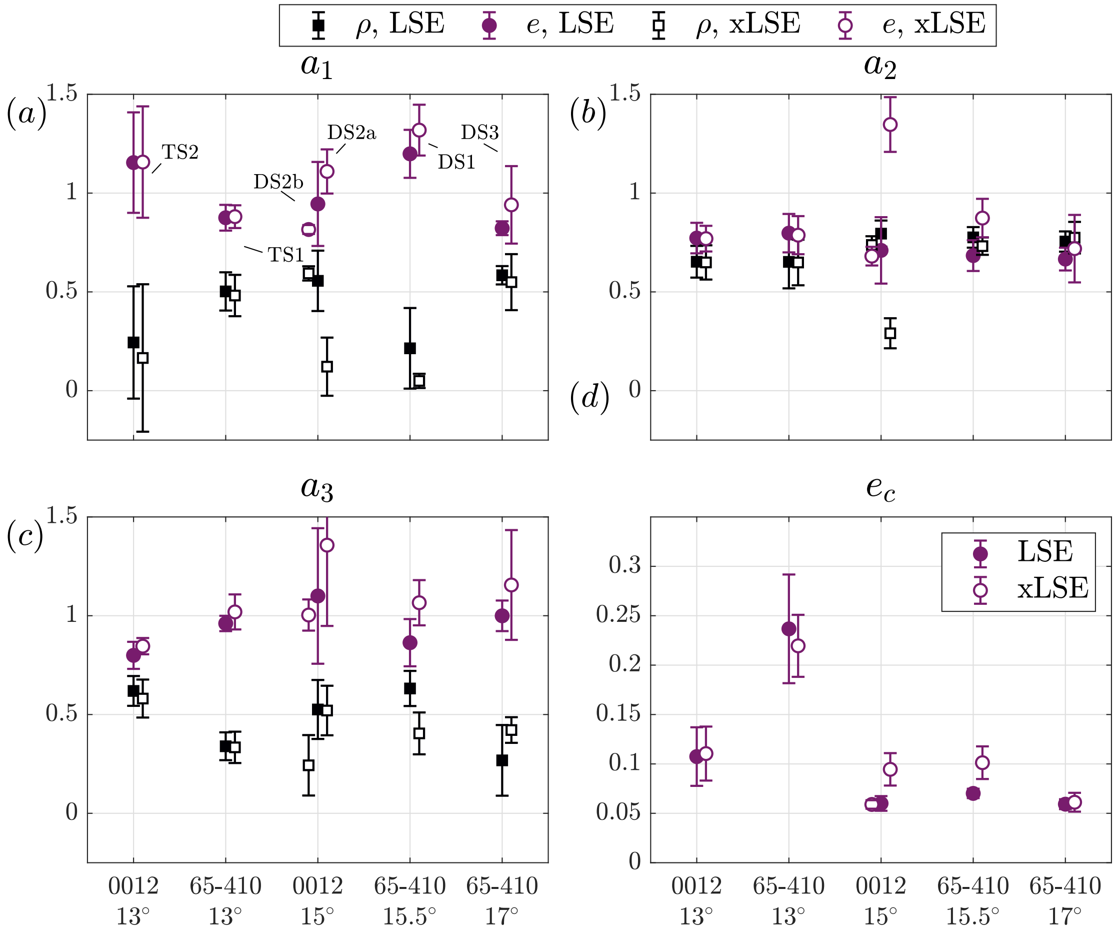

Fig. 10 Correlation and error metrics (equations 4 and 5) for the first three modes (a,b,c) and for the centroid of the separated region (equation 6) in the low order reconstruction (d) for LSE (filled symbols) and xLSE (offset open symbols). Error bars correspond to 95% confidence interval.

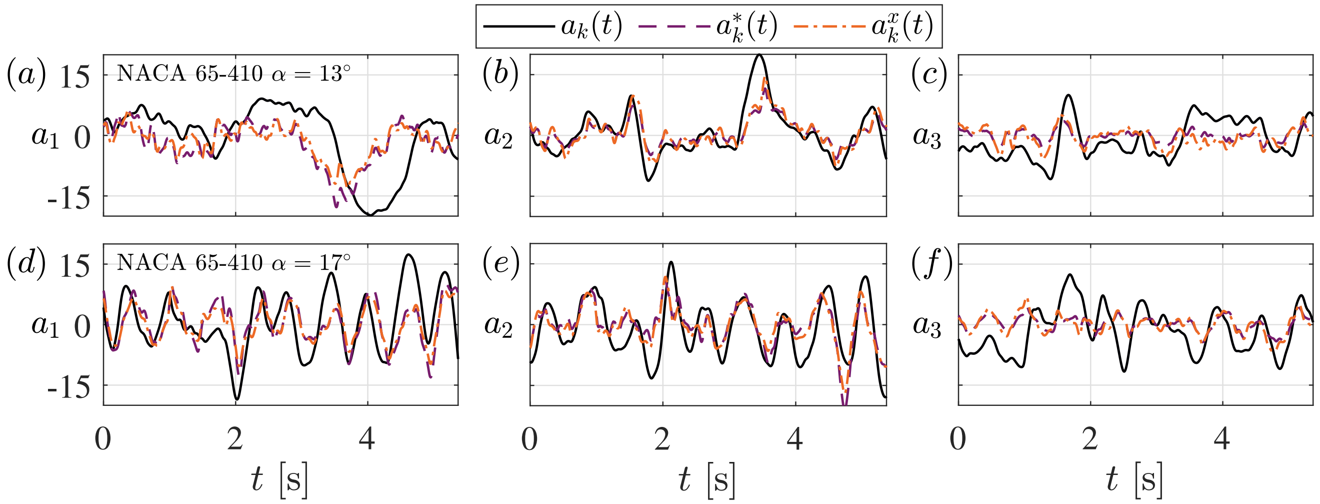

Fig. 11 Real POD coefficients (black), LSE (dashed purple), and xLSE (dashed-dot orange) for the transitionally stalled NACA 65-410 at $\alpha = 13°$ (a-c, case TS1 for the xLSE) and fully stalled NACA 65-410 at $\alpha = 17°$ (d-f, case DS3 for the xLSE) for the first (a,d), second (b,e) and third (c,f) mode coefficients.

where $\tilde{\boldsymbol{B}}$ is the LSE coefficients (see Appendix A) from a library of training data with a different airfoil geometry and $\boldsymbol{S}$ is a diagonal sign-correction matrix with entries of ±1 to adjust for the arbitrary sign of the spatial velocity modes. Each diagonal element of $\boldsymbol{S}$ (corresponding to each mode) is obtained from the sign of the (overlapping) spatial cross-correlation between the POD modes of both cases [see 45].

It is noted that using a library based on a TS case to predict a DS is not included in table 2. This was tested (not presented) and found to fail to predict the coefficients. This is because xLSE is motivated primarily by the similarity in the spectral content and spatial structure of modes between cases. Therefore, the presented applications of xLSE are restricted to cases with similar spectral content (figure 5).

The xLSE results are shown in figure 10 (open symbols). Overall, the xLSE performs similarly to the standard LSE. This is supported by the overlapping uncertainty in the error and correlations for most modes and cases. The xLSE offered no significant improvement e.g. in the difficult TS case of the NACA 65-410 at $\alpha = 13°$, where the centroid error remains near 25%. The similarity in the xLSE with the LSE can be seen from inspection of figure 11.

Though the application of LSE and xLSE is used here for the purpose of instantaneous state estimation, the present results lend valuable insight on the low-order dynamics of separated airfoils in general. Evidently, the dynamics of the symmetric and cambered airfoils are similar enough to yield comparable accuracy in the low-order state estimation. This suggests that low-order dynamics of stalled airfoils may have universal features independent of airfoil geometry. At the same time, such features are strongly dependent on the stability of the system with angle of attack (i.e. TS vs DS).

V. Conclusions

A data-driven analysis has been presented for symmetric and cambered NACA 0012 and NACA 65-410 airfoils at $Re_c = 7.1 \times 10^4$ in transient stall (TS) and deep stall (DS) flow regimes. The spectral peak characterising the flow for the TS and DS cases are found at a Strouhal number $St^\star \approx 0.03$ and $St^\star \approx 0.15$ respectively. This was identified in the lift forces from load cell measurements and via the POD of the PIV in both the velocity and pressure fields. These frequencies are in excellent agreement with previous experimental and numerical studies for symmetric and cambered airfoils [14, 26, 29, 31].

Using a simplified POD-based model that retains only three modes, the stall mechanisms for both TS and DS cases were elucidated at their corresponding dominant Strouhal frequency. For the TS cases, the frequency $St^\star \approx 0.03$ was shown to be the signature of non-linear separation and reattachment under TE stall (figure 9). For the DS cases, the frequency $St^\star \approx 0.15$ was shown to be associated to the bluff body vortex shedding under LE stall (figure 8).

Motivated by flow determination from surface-mounted sensors, the instantaneous planar pressure reconstructions were leveraged to perform a pseudo-probe analysis using 3 sensors at $x/c = 0, 0.5$, and 1, and LSE-POD to reconstruct the low-order velocity fields. The mode coefficients were predicted with an average correlation of $\rho \approx 0.5$, but typically underestimated the magnitude of the coefficients resulting in $e \approx 1$ (figure 11). Despite the difficulty, the centroid of the reverse flow region was predicted to an accuracy of about 5% of the chord for cases in DS and with 10-25% accuracy for the TS cases.

Throughout the present analysis, the observations between the symmetric and cambered airfoils were strikingly consistent depending on whether the flow was in TS or DS. This is is readily seen in the shape of the spatial modes (figure 7). Such similarity motivated the so-called cross LSE (xLSE) to predict the state of the flow using three sensors whose LSE coefficients are trained from a library of correlations of an airfoil with the opposite camber symmetry. The xLSE predictions were generally very close to the standard LSE, indicating that the low order dynamics are not sensitive to the airfoil camber (at least for the two geometries presented). As the spectral characteristics of the flows clearly manifest in the time-variation of the dominant POD modes (figure 6), the agreement in the LSE and xLSE confirms high similarity in the low order dynamics of both symmetric and cambered airfoils.

The present work substantiates the ever-growing body of literature on the complex dynamics of airfoil stall mechanisms at moderate to high Reynolds numbers. The flexibility of the LSE to predict the low order dynamics independent of the exact airfoil geometry is a promising avenue of research, with the potential for a universal set of LSE coefficients for predicting the stall state of airfoils in real time. This potential capability is relevant to a wealth of engineering applications that benefit from feedback control.

Appendix A: LSE-POD Implementation

For each case, the data is divided into four runs corresponding to the "training" data and one run for testing. The training data is sub-sampled to one in every 25 samples and used to determine the LSE coefficients for the low-order velocity field reconstruction using the testing data. In general, the probe correlation matrix $\boldsymbol{W}$ is obtained as

$$\boldsymbol{W} = \begin{bmatrix} \langle P_1 P_1 \rangle & \dots & \langle P_{N_p} P_1 \rangle \\ \vdots & \ddots & \vdots \\ \langle P_1 P_{N_p} \rangle & \dots & \langle P_{N_p} P_{N_p} \rangle \end{bmatrix}. \tag{8}$$

Here P_k is the k-th fluctuating pressure probe signal with $N_p = 3$ the number of probes. The angled brackets denote the average over the number of training samples $N_t = 860$ for each case. The probe-mode cross-correlation matrix $\boldsymbol{V}$ is constructed as

$$\boldsymbol{V} = \begin{bmatrix} \langle P_1 a_1 \rangle & \dots & \langle P_{N_p} a_1 \rangle \\ \vdots & \ddots & \vdots \\ \langle P_1 a_K \rangle & \dots & \langle P_{N_p} a_K \rangle \end{bmatrix} \tag{9}$$

where for the present low-order reconstruction the number of modes $K = 3$. Using the probe correlation and probe-mode cross-correlation matrices the LSE coefficients are obtained as

$$\boldsymbol{B} = \boldsymbol{W}^{-1}\boldsymbol{V}. \tag{10}$$

Equation 10 minimizes the mean-square error between the POD coefficients and their estimate in the training data [48, 71]. Using the testing data, the reconstruction of the POD coefficients at any instant is obtained via

$$a_k^*(t) = P_i(t) B_{ik}. \tag{11}$$

A low-order reconstruction of the velocity fields over the first three modes is then obtained via

$$\boldsymbol{u}^*(\boldsymbol{x}, t) = \sum_{k=1}^{3} a_k^*(t) \boldsymbol{\phi}_k^{uv}(\boldsymbol{x}) + \boldsymbol{U}(\boldsymbol{x}). \tag{12}$$

Acknowledgments

The authors are grateful for financial support from the Engineering and Physical Sciences Research Council (Ref No: EP/R010900/1) and H2020 Future and Emerging Technologies Project HOMER 769237. The authors acknowledge J. Lawson whose MATLAB code for PIV processing is available at: https://git.soton.ac.uk/jml1g18/pivtools

Data Availability

All data and figures presented in this study will be openly available from the University of Southampton repository upon publication.

Competing Interests

The authors report no conflict of interest.

References

[1] Jones, B. M., "Stalling," *The Aeronautical Journal*, Vol. 38, No. 285, 1934, pp. 753–770.

[2] Crabtree, L., *The formation of regions of separated flow on wing surfaces*, Citeseer, 1959.

[3] Gault, D. E., "A correlation of low-speed, airfoil-section stalling characteristics with Reynolds number and airfoil geometry," Tech. rep., 1957.

[4] Gaster, M., "The structure and behaviour of separation bubbles," 1967.

[5] Tani, I., "Low-speed flows involving bubble separations," *Progress in Aerospace Sciences*, Vol. 5, 1964, pp. 70–103.

[6] Morris, W. J., and Rusak, Z., "Stall onset on aerofoils at low to moderately high Reynolds number flows," *Journal of Fluid Mechanics*, Vol. 733, 2013, pp. 439–472.

[7] Wu, W., Meneveau, C., and Mittal, R., "Spatio-temporal dynamics of turbulent separation bubbles," *Journal of Fluid Mechanics*, Vol. 883, 2020.

[8] Mccullough, G. B., and Gault, D. E., "Examples of three representative types of airfoil-section stall at low speed," Tech. rep., 1951.

[9] Sandham, N., "Transitional separation bubbles and unsteady aspects of aerofoil stall," *The Aeronautical Journal*, Vol. 112, No. 1133, 2008, pp. 395–404.

[10] Mulleners, K., and Raffel, M., "The onset of dynamic stall revisited," *Experiments in fluids*, Vol. 52, No. 3, 2012, pp. 779–793.

[11] Le Fouest, S., Deparday, J., and Mulleners, K., "The dynamics and timescales of static stall," *Journal of Fluids and Structures*, Vol. 104, 2021, p. 103304.

[12] Lacagnina, G., Chaitanya, P., Berk, T., Kim, J.-H., Joseph, P., Ganapathisubramani, B., Hasheminejad, S. M., Chong, T. P., Stalnov, O., Choi, K.-S., et al., "Mechanisms of airfoil noise near stall conditions," *Physical Review Fluids*, Vol. 4, No. 12, 2019, p. 123902.

[13] Turner, J. M., and Kim, J. W., "Aerofoil dipole noise due to flow separation and stall at a low Reynolds number," *International Journal of Heat and Fluid Flow*, Vol. 86, 2020, p. 108715.

[14] Busquet, D., Marquet, O., Richez, F., Juniper, M., and Sipp, D., "Bifurcation scenario for a two-dimensional static airfoil exhibiting trailing edge stall," *Journal of Fluid Mechanics*, Vol. 928, 2021.

[15] Counsil, J. N., and Goni Boulama, K., "Low-reynolds-number aerodynamic performances of the NACA 0012 and Selig–Donovan 7003 Airfoils," *Journal of aircraft*, Vol. 50, No. 1, 2013, pp. 204–216.

[16] Zhang, W., Cheng, W., Gao, W., Qamar, A., and Samtaney, R., "Geometrical effects on the airfoil flow separation and transition," *Computers & Fluids*, Vol. 116, 2015, pp. 60–73.

[17] Thomareis, N., and Papadakis, G., "Effect of trailing edge shape on the separated flow characteristics around an airfoil at low Reynolds number: A numerical study," *Physics of Fluids*, Vol. 29, No. 1, 2017, p. 014101.

[18] Boutilier, M. S., and Yarusevych, S., "Effects of end plates and blockage on low-Reynolds-number flows over airfoils," *AIAA journal*, Vol. 50, No. 7, 2012, pp. 1547–1559.

[19] Istvan, M. S., Kurelek, J. W., and Yarusevych, S., "Turbulence intensity effects on laminar separation bubbles formed over an airfoil," *AIAA Journal*, Vol. 56, No. 4, 2018, pp. 1335–1347.

[20] Brücker, C., and Weidner, C., "Influence of self-adaptive hairy flaps on the stall delay of an airfoil in ramp-up motion," *Journal of Fluids and Structures*, Vol. 47, 2014, pp. 31–40.

[21] Pérez-Torró, R., and Kim, J. W., "A large-eddy simulation on a deep-stalled aerofoil with a wavy leading edge," *Journal of Fluid Mechanics*, Vol. 813, 2017, pp. 23–52.

[22] Hristov, G., and Ansell, P. J., "Poststall hysteresis and flowfield unsteadiness on a naca 0012 airfoil," *AIAA journal*, Vol. 56, No. 7, 2018, pp. 2528–2539.

[23] Brunner, C. E., Kiefer, J., Hansen, M. O., and Hultmark, M., "Study of Reynolds number effects on the aerodynamics of a moderately thick airfoil using a high-pressure wind tunnel," *Experiments in Fluids*, Vol. 62, No. 8, 2021, pp. 1–17.

[24] Leishman, J. G., and Beddoes, T., "A Semi-Empirical model for dynamic stall," *Journal of the American Helicopter society*, Vol. 34, No. 3, 1989, pp. 3–17.

[25] Greenblatt, D., and Wygnanski, I., "Effect of leading-edge curvature on airfoil separation control," *Journal of Aircraft*, Vol. 40, No. 3, 2003, pp. 473–481.

[26] Zaman, K., McKinzie, D., and Rumsey, C., "A natural low-frequency oscillation of the flow over an airfoil near stalling conditions," *Journal of Fluid Mechanics*, Vol. 202, 1989, pp. 403–442.

[27] Swalwell, K. E., Sheridan, J., Melbourne, W., et al., "The effect of turbulence intensity on stall of the NACA 0021 aerofoil," *14th Australasian fluid mechanics conference*, 2001, pp. 941–944.

[28] Huang, R. F., and Lee, H. W., "Turbulence effect on frequency characteristics of unsteady motions in wake of wing," *AIAA journal*, Vol. 38, No. 1, 2000, pp. 87–94.

[29] ElAwad, Y. A., and ElJack, E. M., "Numerical investigation of the low-frequency flow oscillation over a NACA-0012 aerofoil at the inception of stall," *International Journal of Micro Air Vehicles*, Vol. 11, 2019, p. 1756829319833687.

[30] Rodríguez, I., Lehmkuhl, O., Borrell, R., and Oliva, A., "Direct numerical simulation of a NACA0012 in full stall," *International journal of heat and fluid flow*, Vol. 43, 2013, pp. 194–203.

[31] Yarusevych, S., Sullivan, P. E., and Kawall, J. G., "On vortex shedding from an airfoil in low-Reynolds-number flows," *Journal of Fluid Mechanics*, Vol. 632, 2009, pp. 245–271.

[32] Burtsev, A., He, W., Hayostek, S., Zhang, K., Theofilis, V., Taira, K., and Amitay, M., "Linear modal instabilities around post-stall swept finite-aspect ratio wings at low Reynolds numbers," *arXiv preprint arXiv:2102.04103*, 2021.

[33] Fage, A., and Johansen, F., "On the flow of air behind an inclined flat plate of infinite span," *Proceedings of the Royal Society of London. Series A, Containing Papers of a Mathematical and Physical Character*, Vol. 116, No. 773, 1927, pp. 170–197.

[34] Roshko, A., "On the drag and shedding frequency of two-dimensional bluff bodies," Tech. rep., 1954.

[35] Derakhshandeh, J., and Alam, M. M., "A review of bluff body wakes," *Ocean Engineering*, Vol. 182, 2019, pp. 475–488.

[36] Sirovich, L., "Turbulence and the dynamics of coherent structures. III. Dynamics and scaling," *Quarterly of Applied mathematics*, Vol. 45, No. 3, 1987, pp. 583–590.

[37] Berkooz, G., Holmes, P., and Lumley, J. L., "The proper orthogonal decomposition in the analysis of turbulent flows," *Annual review of fluid mechanics*, Vol. 25, No. 1, 1993, pp. 539–575.

[38] Taira, K., Brunton, S. L., Dawson, S. T., Rowley, C. W., Colonius, T., McKeon, B. J., Schmidt, O. T., Gordeyev, S., Theofilis, V., and Ukeiley, L. S., "Modal analysis of fluid flows: An overview," *Aiaa Journal*, Vol. 55, No. 12, 2017, pp. 4013–4041.

[39] Wu, J.-Z., Lu, X.-Y., Denny, A. G., Fan, M., and Wu, J.-M., "Post-stall flow control on an airfoil by local unsteady forcing," *Journal of Fluid Mechanics*, Vol. 371, 1998, pp. 21–58.

[40] Pinier, J. T., Ausseur, J. M., Glauser, M. N., and Higuchi, H., "Proportional closed-loop feedback control of flow separation," *AIAA journal*, Vol. 45, No. 1, 2007, pp. 181–190.

[41] Nair, A. G., Yeh, C.-A., Kaiser, E., Noack, B. R., Brunton, S. L., and Taira, K., "Cluster-based feedback control of turbulent post-stall separated flows," *Journal of Fluid Mechanics*, Vol. 875, 2019, pp. 345–375.

[42] Déda, T. C., and Wolf, W. R., “Extremum seeking control applied to airfoil trailing-edge noise suppression,” *AIAA Journal*, Vol. 60, No. 2, 2022, pp. 823–843.

[43] Jayaraman, B., Al Mamun, S., and Lu, C., “Interplay of Sensor Quantity, Placement and System Dimension in POD-based Sparse Reconstruction of Fluid Flows,” *Fluids*, Vol. 4, No. 2, 2019, p. 109.

[44] Manohar, K., Brunton, B. W., Kutz, J. N., and Brunton, S. L., “Data-driven sparse sensor placement for reconstruction: Demonstrating the benefits of exploiting known patterns,” *IEEE Control Systems Magazine*, Vol. 38, No. 3, 2018, pp. 63–86.

[45] Carter, D. W., De Voogt, F., Soares, R., and Ganapathisubramani, B., “Data-driven sparse reconstruction of flow over a stalled aerofoil using experimental data,” *Data-Centric Engineering*, Vol. 2, 2021.

[46] Callaham, J. L., Maeda, K., and Brunton, S. L., “Robust flow reconstruction from limited measurements via sparse representation,” *Physical Review Fluids*, Vol. 4, No. 10, 2019, p. 103907.

[47] Adrian, R. J., “Stochastic estimation of the structure of turbulent fields,” *Eddy structure identification*, Springer, 1996, pp. 145–195.

[48] Murray, N. E., and Ukeiley, L. S., “Estimation of the flowfield from surface pressure measurements in an open cavity,” *AIAA journal*, Vol. 41, No. 5, 2003, pp. 969–972.

[49] Lasagna, D., Orazi, M., and Iuso, G., “Multi-time delay, multi-point linear stochastic estimation of a cavity shear layer velocity from wall-pressure measurements,” *Physics of Fluids*, Vol. 25, No. 1, 2013, p. 017101.

[50] Taylor, J., and Glauser, M. N., “Towards practical flow sensing and control via POD and LSE based low-dimensional tools,” *J. Fluids Eng.*, Vol. 126, No. 3, 2004, pp. 337–345.

[51] Durgesh, V., and Naughton, J., “Multi-time-delay LSE-POD complementary approach applied to unsteady high-Reynolds-number near wake flow,” *Experiments in fluids*, Vol. 49, No. 3, 2010, pp. 571–583.

[52] Podvin, B., Nguimatsia, S., Foucaut, J.-M., Cuvier, C., and Fraigneau, Y., “On combining linear stochastic estimation and proper orthogonal decomposition for flow reconstruction,” *Experiments in Fluids*, Vol. 59, No. 3, 2018, pp. 1–12.

[53] Westphal, W. R., *Comparison of NACA 65-series Compressor-blade Pressure Distributions and Performance in a Rotor and in Cascade*, National Advisory Committee for Aeronautics, 1951.

[54] Scherl, I., Strom, B., Shang, J. K., Williams, O., Polagye, B. L., and Brunton, S. L., “Robust principal component analysis for modal decomposition of corrupt fluid flows,” *Physical Review Fluids*, Vol. 5, No. 5, 2020, p. 054401.

[55] Lin, Z., Chen, M., and Ma, Y., “The augmented lagrange multiplier method for exact recovery of corrupted low-rank matrices,” *arXiv preprint arXiv:1009.5055*, 2010.

[56] Sobral, A., Bouwmans, T., and Zahzah, E.-h., “Lrslibrary: Low-rank and sparse tools for background modeling and subtraction in videos,” *Robust Low-Rank and Sparse Matrix Decomposition: Applications in Image and Video Processing*, 2016.

[57] Adrian, R. J., and Westerweel, J., *Particle image velocimetry*, 30, Cambridge university press, 2011.

[58] Raffel, M., Willert, C., Scarano, F., Kähler, C., Wereley, S., and Kompenhans, J., "Particle Image Velocimetry: A Practical Guide, Third edit," , 2018.

[59] De Kat, R., and Van Oudheusden, B., "Instantaneous planar pressure determination from PIV in turbulent flow," *Experiments in fluids*, Vol. 52, No. 5, 2012, pp. 1089–1106.

[60] Laskari, A., de Kat, R., and Ganapathisubramani, B., "Full-field pressure from snapshot and time-resolved volumetric PIV," *Experiments in fluids*, Vol. 57, No. 3, 2016, p. 44.

[61] Van Gent, P., Michaelis, D., Van Oudheusden, B., Weiss, P.-É., de Kat, R., Laskari, A., Jeon, Y. J., David, L., Schanz, D., Huhn, F., et al., "Comparative assessment of pressure field reconstructions from particle image velocimetry measurements and Lagrangian particle tracking," *Experiments in Fluids*, Vol. 58, No. 4, 2017, p. 33.

[62] Jakobsen, M., Dewhirst, T., and Greated, C., "Particle image velocimetry for predictions of acceleration fields and force within fluid flows," *Measurement Science and Technology*, Vol. 8, No. 12, 1997, p. 1502.

[63] Ragni, D., Ashok, A., Van Oudheusden, B., and Scarano, F., "Surface pressure and aerodynamic loads determination of a transonic airfoil based on particle image velocimetry," *Measurement Science and technology*, Vol. 20, No. 7, 2009, p. 074005.

[64] Van Oudheusden, B., "PIV-based pressure measurement," *Measurement Science and Technology*, Vol. 24, No. 3, 2013, p. 032001.

[65] Villegas, A., and Diez, F., "Evaluation of unsteady pressure fields and forces in rotating airfoils from time-resolved PIV," *Experiments in fluids*, Vol. 55, No. 4, 2014, pp. 1–17.

[66] McCroskey, W. J., "The phenomenon of dynamic stall." Tech. rep., National Aeronuatics and Space Administration Moffett Field Ca Ames Research . . . , 1981.

[67] Chatterjee, A., "An introduction to the proper orthogonal decomposition," *Current science*, 2000, pp. 808–817.

[68] Mikhaylov, K., Rigopoulos, S., and Papadakis, G., "Reconstruction of large-scale flow structures in a stirred tank from limited sensor data," *AIChE Journal*, Vol. 67, No. 10, 2021, p. e17348.

[69] Adrian, R. J., "On the role of conditional averages in turbulence theory," 1975.

[70] Cole, D. R., Glauser, M. N., and Guezennec, Y. G., "An application of the stochastic estimation to the jet mixing layer," *Physics of Fluids A: Fluid Dynamics*, Vol. 4, No. 1, 1992, pp. 192–194.

[71] Tinney, C., Coiffet, F., Delville, J., Hall, A., Jordan, P., and Glauser, M., "On spectral linear stochastic estimation," *Experiments in fluids*, Vol. 41, No. 5, 2006, pp. 763–775.